Silicon optrode with a micromirror-tip providing tunable beam profile during infrared neuromodulation of the rat neocortex

Ágoston Csaba Horváth[1], Ákos Mórocz [1], Borbála Csomai [1], Ágnes Szabó [1], Zsófia Balogh-Lantos [1], Péter Fürjes[2], Estilla Zsófia Tóth[3], Richárd Fiáth [1,3], Zoltán Fekete[1,4]

1 Research Group for Implantable Microsystems, Faculty of Information Technology & Bionics, Pázmány Peter Catholic University, Budapest, Hungary

2 Microsystems Laboratory, Institute for Technical Physics & Material Science, Center for Energy Research, Budapest, Hungary

3 Integrative Neuroscience Research Group, Institute for Cognitive Neuroscience & Psychology, Research Center for Natural Sciences, Budapest, Hungary

4 Sleep Oscillation Research Group, Institute for Cognitive Neuroscience & Psychology, Research Center for Natural Sciences, Budapest, Hungary

Abstract

Infrared (IR) neuromodulation holds an increasing potential in brain research, which is fueled by novel neuroengineering approaches facilitating the exploration of the biophysical mechanism in the microscale. Our group lays down the fundamentals of spatially controlled optical manipulation of inherently temperature sensitive neuronal population. The concept and in vivo validation of a multifunctional, optical stimulation microdevice is presented, which expands the capabilities of conventional optrodes by coupling IR light through a monolithically integrated parabolic micromirror. Heat distribution in the irradiated volume is experimentally analyzed, and performance of the integrated electrophysiological recording components of the device are tested in the neocortex of anaesthetized rodents. Evoked single cell responses upon IR irradiation through the novel microtool are evaluated in multiple trials. The safe operation of the implanted device is also presented using immunohistological methods. Our results confirm that shift in temperature distribution in the vicinity of the optrode tip can be controlled by the integrated photonic components, and in parallel with the optical stimulation, the device is suitable to interrogate the evoked electrophysiological activity at the single neuron level. Our customizable and scalable optrode system provides a new pathway to tailor the location of the heat maximum during infrared neural stimulation.

1 Introduction

In the last decade, optical stimulation methods have been routinely used to modulate the activity of neural cells within the brain tissue. A groundbreaking technology, optogenetics, laid down the fundamentals of stimulation approaches aiming to address specific cell populations due to genetic incorporation of light-sensitive proteins into the cell membrane [Yizhar, 2011]. The selective expression of these molecular transducers in the tissue inherently fueled the development of novel, implantable tools that provided spatially addressable optical stimulation. Besides the transmission of light waves to the tissue, the interrogation of evoked electrical activity of the irradiated cells was also important, which triggered further development of multifunctional devices that combines optical stimulation with electrophysiology in a single, integrated instrument [Fan, 2015; Tian, 2022]. The widespread use of the technology of microelectromechanical systems (MEMS) facilitated the implementation of microscale configurations where the stimulation spot and the location of electrical recording sites can be positioned with respect to each other with microscale precision [Fekete, 2015]. By configuration, two conceptual pathways are in use to realize such stimulation devices. Passive devices rely on external light sources that are combined with integrated photonic components to the target tissue [Wu, 2013; Shim, 2016; Sacher, 2021; Horváth 2020], while active devices hold chip-scale light sources, e.g. microLEDs or laser diodes on the implanted regions to locally provide the necessary illumination profile [Wu, 2015; Schwaerzle 2017; Reddy, 2019; Kim, 2020; Yasunaga, 2022]. One of the first passive approaches was reported by Royer et al., who fixed an optical fiber on top of a silicon neural probe to transmit blue light for optogenetic experiments, while recorded the response of the stimulated neuronal population by the integrated recording sites of the probe [Royer, 2010]. Later on, Wu and colleagues presented a micromachining process on how integrated dielectric thin-film waveguides of oxynitride core and silicon-dioxide cladding can be formed to complement electrophysiology modalities of silicon probes with optical stimulation sites [Wu, 2013]. Since then, several approaches have been presented that were based on similar surface micromachining techniques [Shim, 2016; Sacher, 2021]. Further improvements have been made by increasing the number of illumination spots in a linear arrangement to provide multisite [Segev, 2016; McAlinden, 2019] or multicolor [Kampasi, 2018; Li, 2022] illumination.

Although planar MEMS technology has successfully promoted the evolution of these multifunctional tools, there were some limitations of the realized configurations in terms of guiding the beam spot in space with respect to the implanted probe. Besides the increasing functional density, the direction of the outcoupled light was also getting important, as the distance between the illumination center and the recording array may lead to improper conclusions on the evoked responses of the monitored cells to the light stimulus. To circumvent this issue, several smart microoptical solutions have been proposed in the literature. Shim et al. proposed grating couplers along silicon-nitride surface waveguides to tailor the illumination spots along a neural probe shaft [Shim, 2016]. Segev et al. employed wavelength division multiplexing modulated by an arrays waveguide grating in combination with a photonic waveguide connected to grating couplers [Segev, 2016]. Another multi-shank silicon probe was developed to provide sheet-like illumination patterns for fluorescence light sheet microscopy conveyed through a grating coupler in the end facet of the probe [Sacher, 2021]. Individually addressable surface waveguides integrated on a probe backbone in conjunction with multimode interferometer-based switches were presented to control the illumination pattern at the tip of the probe [Mohanty, 2020]. Optical ring resonators located along the probe shaft have been also used to spatially change the location of the light output by making small (< 1 nm) shifts in the wavelength of the external light source [Lanzio, 2021]. Besides silicon-based solutions, tapered fibers nanomachined by focused ion beam milling to form optical output windows and recording sites have been also proposed [Spagnolo, 2022]. It should also be noted that these modifications of the end facet

of the neural probe can also be effective to replace gradient index (GRIN) lenses and prisms of higher form factor in the case of several deep tissue microscopy techniques [Sacher, 2021].

However, these approaches were proved to be suitable to excite or suppress the activity of genetically modified neurons, the dimensions of the microoptical components limit the power density that can be achieved on the illumination spot. This is especially important if, unlike in the case of optogenetics, the water content of the tissue is acting as chromophore, and the heat converted through light absorption is responsible for the evoked neuronal response. The technique relying on this mechanism is called infrared neuromodulation, which does not utilize genetically engineered proteins, but endogenously expressed heat sensitive ion channels [Chernov, 2014; Fekete 2020]. In this case, surface micromachined approaches do not provide sufficient elevation in tissue temperature. The potential technical solution was proposed by the Solzbacher group, who transformed the silicon needles of a Utah electrode array into optical waveguides for infrared (IR) transmission [Abaya, 2012], however, due to high propagation loss, these devices have never been tested among in vivo conditions. The first Michigan-type neural probe for IR stimulation was developed by our group. Using a wet chemical polishing technique, our process transformed the probe shaft from a simple mechanical carrier into an infrared waveguide [Kiss, 2016; Horváth, 2018]. The monolithic integration of the waveguide, the electrophysiology and temperature sensor elements integrated into a single implantable microdevice effectively contributed to the in vivo evaluation of IR stimulation and inhibition within the neocortex and the hippocampus of rats [Horváth, 2020; Horváth, 2022]. In the present paper, we substantially improved this device concept to give freedom to control the direction of the light coupled out from the waveguide. While the dimensions and layout are fully customizable, the technology is compatible with mass manufacturing processes. A monolithically integrated parabolic micromirror is guiding the illumination spot to provide thermal excitation confined to individual layers of the neocortex. Besides electrical and optical/thermal characterization of the microdevice, our work gives evidence on the controlled asymmetric heating profile next to the probe shaft by showing the results of in vivo electrophysiology including evoked neuronal responses. Beyond proving the efficacy of the modulation of neural activity, the safety of IR stimulation with our device will also be presented by an immunohistological analysis of the stimulated tissue region.

2   Methods

2.1   Optrode design

The design of the silicon-based optrode was expected to meet multiple requirements. It was necessary (1) to perform electrical recordings and optical stimulation in parallel, (2) to be implantable into the brain tissue, and (3) to be able to effectively shape the IR beam emitted at the probe tip.

The current length, width and thickness of the silicon shaft are 4.7 mm, 170 µm and 200 µm, respectively. We also note that these dimensions are customizable, with the flexibility to adapt to the requirements of individual applications (e.g. increased length for animal models with larger brain sizes). On the top side of the shaft there is a linear array of 16 rectangular platinum (Pt) electrophysiological recording sites with 100 µm spacing in between. Each recording site has a side length of 30 µm. The backbone of the chip (3.5 mm×3.5 mm; cf. Fig. 1. A, C) holds bonding bands for electrical microwires and a dry-etched groove to support the insertion of a glass optical fiber. To shape the emitting profile, a tip ending in a parabolic micromirror was designed. The mathematical representation of this parabolic curve is a section between 200 to 370 of a parabola with parameter p=−200. This means that an arbitrary point P along the parabolic curve has the Cartesian coordinates P=(y;x), where:

$$x = \frac{1}{2p} y^2, \tag{1}$$

i.e.

$$x = -\frac{1}{400} y^2, \tag{2}$$

where $200 \leq y \leq 370$. This parabolic arc provides a reflective surface for the IR beams propagating within the silicon shaft. When most of the IR beams reach the parabolic silicon surface of the tip, the angle of incidence ('θ_i') exceeds the critical angle ('θ_c') of the Si/air or Si/tissue medium boundary, consequently the conditions for total internal reflection are met (cf. Fig. 1. B). This parabolic arc acts as a micromirror and reflects a big part of the incident IR beams to the opposite side of the waveguide. The reflected beams are then coupled out through the optically smooth surface orthogonally with respect to the axis of the optrode (cf. Fig. 1. B). For details of the mathematical and experimental underpinnings of the theoretical summary mentioned here, see [Kiss, 2016], which paper is about measurements on optical dummies.

Regarding the fabrication technology of the multimodal optrode, our previous work gives a detailed overview [Horváth, 2020], therefore, only a brief description is provided here. Single crystalline, p-type doped silicon (Si) wafers were used as initial substrate of our multimodal brain implants. The top and bottom side of the 200 µm thick wafers were polished to be atomically smooth. Sputtered and photolithographically defined metallic layers (Ti/Pt) were embedded in between low-pressure chemical vapor deposition (LPCVD) deposited stacks of silicon-dioxide and silicon-nitride. The metallic layer provided the recording sites, wires and bonding pads of the optrode chip. The final shape of optrode (cf. Fig. 1. C) was released via deep reactive ion etching (DRIE). Alkaline-based wet chemical polishing of the chip was then applied to smooth the scalloping sidewalls remaining after DRIE, which facilitated the use of the silicon shaft as a bulk waveguide [Kiss, 2016]. The optrode chip was mounted on a custom printed circuit board holding a 32-channel miniature Omnetics connector (type: A79022-001, Omnetics Inc.) for transmission of the recorded brain electrical signal. The laser light was coupled to the chip through a glass optical fiber (NA = 0.22) ending in a SMA connector that facilitates interconnection to the laser source.
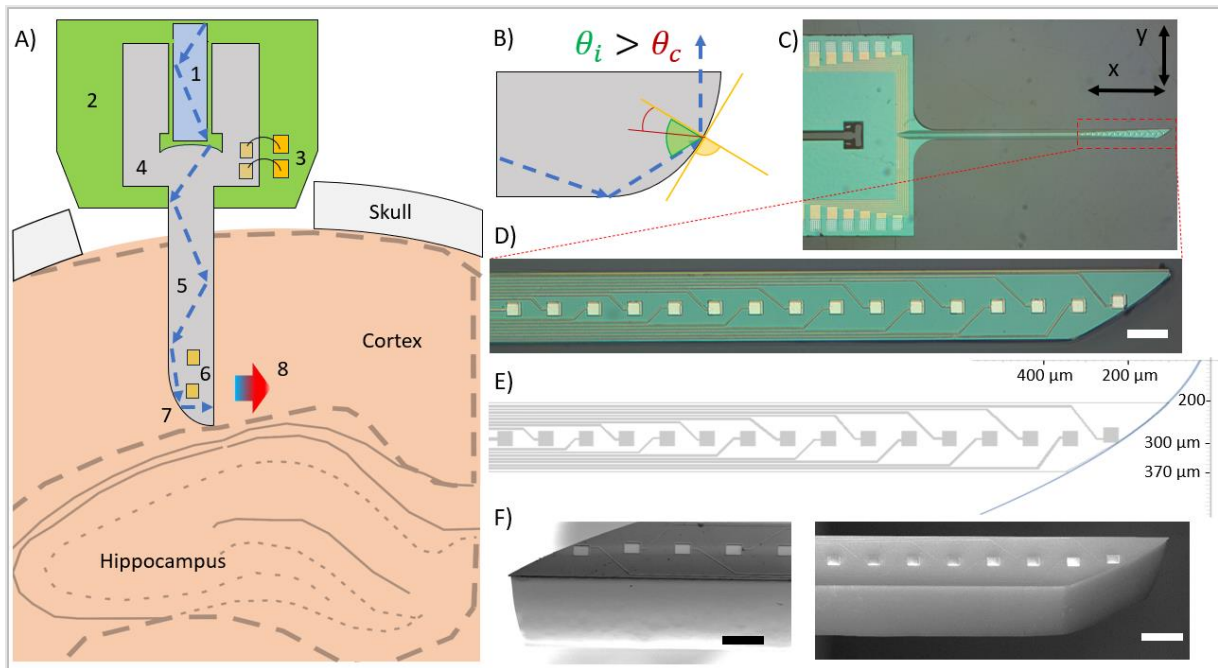
Figure 1: A) Schematic drawing of the principle of operation of the IR optrode. 1: IR light is first guided within a multimode optical fiber; 2: Mechanical carrier (PCB) of the implant; 3: Microwire bonding provides electrical interconnect; 4: Cylindrical lens helps coupling and collimating IR light from the fiber to the Si needle; 5: Si shaft as electrode substrate and IR waveguide; 6: Electrophysiological recording sites; 7: Parabolic micromirror; 8: IR light exiting the optrode heats the tissue. Image is not to scale. B) Schematic drawing explaining the specular property of the optrode tip through the principle of total internal reflection. C) Optical microscopy view of the multimodal Si chip. Arrows in black define the two perpendicular axes along which the distribution of optical heating was investigated (cf. 2.2.2 & 3.2.) and act as scale bars as well: x=1.6 mm, y=1.3 mm. D) Magnified optical microscopy view of the Si needle. Light squares in a row are platinum electrophysiological recording sites. E) Portion of the scaled technical drawing of the design. F) Scanning electron microscopy (SEM) images of the vicinity of the Si tip with the same scale of panel D. Scale bars on panels D & F mean 100 µm.

2.2   Testing of integrated functionalities

2.2.1   Electrochemical characterization and deposition

The electrochemical impedance spectroscopy (EIS) method was applied to characterize the integrated Pt sites of our optrode. The three-electrode electrochemical test cell was set up within a Faraday cage. A Gamry Reference 600 Potentiostat (Gamry Instruments, Warminster, PA, USA) measured the potential change of each Pt site connected to its working electrode pin. The counter and reference electrodes were a Pt wire and an Ag/AgCl electrode, respectively (the reference electrode was kept in 3 M KCl solution; MF-2056, BASi Inc, IN, USA). A 25 mV_{RMS} sinusoidal AC voltage was applied between the working and the counter electrode, and it was swept between 1 Hz to 10 kHz in 0.01 M phosphate buffered saline (P4417, tablet diluted in 200 ml deionized water, Merck KGaA, Germany) at room temperature. To improve the electrode capacitance, thus reducing impedance, an additional layer of porous platinum was electroplated on the sputtered platinum recording sites [Márton, 2014]. The increased specific surface area of the electrodes contributes to a higher signal-to-noise ratio during the electrophysiological recordings [Kozai, 2015]. The electrochemical deposition of the porous platinum layer was carried out in a Faraday cage by a nanoZ Impedance Tester instrument (White Matter LLC, Seattle, WA, USA) using its 'DC electroplate' mode. A level of -0.09 µA DC plating current was driven through each recording site for 60 seconds. The electrolyte solution was a lead free 1 wt.% chloroplatinic acid solution (diluted from 8 wt.% chloroplatinic acid solution in H_2O, Merck KGaA, Germany) with PVP (Polyvinylpyrrolidone, Merck KGaA, Germany) to improve the wettability of the sputtered Pt surfaces. During the electroplating sequence the same Ag/AgCl reference electrode was

used (MF-2056, BASi Inc, IN, USA). The same nanoZ Impedance Tester instrument was used for a long-term soaking test. The shaft of the optrode under test was immersed in phosphate buffered saline for 7 days and impedance measurement of all 16 recording sites was performed at 1 kHz twice a day.

2.2.2 Bench-top characterization of the optically induced heating

The functionality of the integrated IR optical waveguide was characterized through a bench top, custom-designed optical heating measurement setup (Supplementary Figure S1). The absorbed IR light was converted to heat in a model medium. Two Si-based probes were immersed in a 2 ml polyethylene cylinder filled with water. The material selection and the amount of water was determined in our previous study on optical-thermal modeling of the optrode in rats [Boros, 2019]. One of the probes was an optrode to be characterized, while the other probe held a calibrated platinum temperature sensor [Horvath, 2018], which measured the temperature elevation in the model medium. The axes of the two probes were set to be orthogonal throughout the experiment. An optical fiber (NA = 0.22) was coupled to the optrode, and IR light (λ=1550 nm) was delivered from a custom pigtailed laser diode (LPSC-1550-FG105LCA-SMA, Thorlabs Inc., USA). In line with the theory of light propagation, the asymmetric tip shape of the optrode corresponds to an asymmetric light emission and heating profile. This expected asymmetry in temperature distribution was investigated through a series of temperature measurements. The Pt temperature sensor was fixed in various positions around the tip of the optrode under test with 100 µm spatial resolution along two perpendicular axes (see Fig. 1. C). Axis X is the axis of the shaft of the optrode, axis Y is perpendicular to it (cf. sup. Fig. S1.). In each position, the IR illumination-induced local heating of water was measured five times through 4-wire resistance measurement of the Pt sensor also immersed in water. The 4-wire resistance measurement method provided the highest precision of measurement. Finally, recorded resistance values were transformed to temperature data through the mathematical formula of the Callendar–Van Dusen equation. Temperature values of the five measurements were then averaged and the average values are plotted on the different heating curves (cf. Fig. 3. B-D).

The IR illumination was controlled by the supply current of the laser diode. The current source was a Keithley 2611B SYSTEM SourceMeter (Keithley Instruments Inc, OH, USA). At each spatial coordinate, five consecutive measurements with a one-minute-long ON period (laser switched on) followed by a one-minute-long OFF period (laser switched off) were applied in DC mode. The actual current level of each measurement series was adjusted to achieve an approximately 2 °C difference in temperature. To characterize the relationship between diode current and temperature elevation, the relative position of the two Si needles was fixed and the laser's supply current level was tuned between 100-400 mA with 20 mA steps. The laser ON and OFF states were not changed.

2.3 Animal surgery and optrode/probe implantation

All in vivo experiments were performed according to the EC Council Directive of September 22, 2010 (2010/63/EU), and all procedures were reviewed and approved by the Animal Care Committee of the Research Centre for Natural Sciences and by the National Food Chain Safety Office of Hungary (license number: PE/EA/672-6/2021). Adult Wistar rats (n = 5; weight: 313.0 g ± 49.6 g, mean ± standard deviation; 3 male) were used for the acute in vivo experiments. A mixture of intraperitoneally administered ketamine (75 mg/kg) and xylazine (10 mg/kg) was used to induce anaesthesia. During the surgery and electrophysiological recordings, supplementary doses of ketamine/xylazine were injected intramuscularly to maintain the depth of anaesthesia. A homeothermic heating pad connected to a temperature controller (Supertech, Pécs, Hungary) was used to keep the physiological body temperature of the animals. After reaching the level of surgical anaesthesia, the head of the rat was fixed in a stereotaxic frame (David Kopf Instruments, Tujunga, CA, USA), then the skin and the connective tissue was removed from the top of the skull. Next, for a subset of rats (n = 4), a cranial

window with a size of about 3 mm × 3 mm was drilled over the left hemisphere (anterior-posterior [AP]: from -1.5 mm to -4.5 mm; medial-lateral [ML]: from 1.5 mm to 4.5 mm; coordinates given with respect to the bregma [Paxinos, 2007]). The dura mater was then carefully pierced with a 34-gauge needle over the insertion sites (somatosensory or parietal association cortex) to reduce brain dimpling during implantation of the optrode and the silicon probe. Before implantation, the recording and stimulation devices were mounted on separate motorized stereotaxic micromanipulators (Robot Stereotaxic, Neurostar, Tübingen, Germany). First, the optrode was inserted into the cortical tissue to a depth of 2 mm with a slow speed (2 µm/s; to decrease the insertion-related mechanical tissue damage [Fiáth, 2019]). Following optrode insertion, a single-shank Neuropixels 1.0 silicon probe (IMEC, Leuven, Belgium) with 960 recording sites was driven into the neocortex at a lateral inclination of 25° from the vertical, relative to the coronal plane (see Supplementary Figure S2). The probe was inserted to a depth of 3-3.5 mm (with the sites located close to the probe tip reaching the hippocampus) at a slow speed (2 µm/s). For three animals, the Neuropixels probe was first inserted anterior to the optrode at a distance of 300 µm, facing the side of the optrode where most of the infrared light is emitted (referred to as "front" position). After the first infrared stimulation session (including ten stimulation trials), the Neuropixels probe was withdrawn and reinserted 300 µm posterior to the optrode where the least light is emitted (referred to as "behind" position). It is important to note that reinsertion of probes had no visible effect on the quality of the recorded neural activity. After reinsertion, the infrared stimulation protocol containing ten stimulation trials was repeated. For the fourth animal, only a single penetration was performed with the Neuropixels probe, where it was placed 300 µm anterior to the optrode. The same optrode and Neuropixels probe were used in all experiments. For a post-mortem histological verification of the recording locations, the silicon shank of the Neuropixels probe was coated with red-fluorescent dye 1,1-dioctadecyl-3,3,3,3-tetramethylindocarbocyanine perchlorate (DiI, D-282, ~10% in ethanol, Thermo Fischer Scientific, Waltham, MA, USA) before insertion. A stainless-steel needle inserted in the nuchal muscle of the animal served as the reference and ground electrode during recordings. During the experiment, room temperature physiological saline solution was dripped regularly into the cranial window to prevent dehydration of the cortical tissue.

For the experiment with the fifth rat (used for histological evaluation), two square-shaped craniotomies with a size of 4 mm × 4 mm were prepared over both hemispheres (AP: from -1.5 mm to -5.5 mm; ML: from 1.5 mm to 5.5 mm on both sides; with respect to the bregma). Then, two optrodes were inserted simultaneously into the neocortex to different locations in mirror symmetry to the bregma, to a depth of 2 mm with a speed of 2 µm/s. The location of the device tracks is summarized in Supplementary Figure S3. Before insertion, the dura mater was carefully punctured over the targeted neocortical sites. After reaching the targeted cortical depth, infrared stimulation was performed with one of the optrodes for approximately 1 hour (see details of the stimulation protocol below), while no stimulation was carried out with the other device (sham). Finally, both optrodes were removed from the brain tissue with an explantation speed of 20 µm/s. This implantation – stimulation – explantation procedure was performed one more time using the same optrodes, resulting in a total of four cortical penetrations (see Supplementary Figure S3).

2.4   In vivo electrophysiological recordings

Brain electrical activity (local field potentials and spiking activity separately) was collected using the Neuropixels recording system and a PXIe-1071 chassis with an MXI-Express interface (National Instruments, Austin, Texas, USA). The neural signals were recorded on 384 channels (selected from a total of 960 recording sites) at a sampling rate of 30 kHz/channel for spiking activity and 2.5 kHz/channel for local field potentials. Data was acquired with a resolution of 10 bit using the SpikeGLX software package (https://billkarsh.github.io/SpikeGLX/). Only the first 384 recording sites

of the Neuropixels probe (bank 0, located closest to the probe tip) were used for data acquisition. Approximately one hour long neuronal data was collected at each brain position. To collect wideband (0.1–7500 Hz) neural activity with the recording sites of the optrode, we used an Intan RHD-2000 electrophysiological recording system (Intan Technologies, Los Angeles, CA, USA). Recordings were acquired with a 32-channel amplifier board at a sampling frequency of 20 kHz/channel and a resolution of 16 bit. Neuropixels probe and optrode recordings were collected simultaneously.

2.5   IR neuromodulation protocol

During the in vivo conditions the pacing of IR laser's current supply was modified compared to the bench top optical heating test cases. At the beginning of the one-hour recording period, a two-minute-long recording without IR exposure was conducted. Following this, a series of ten repetitions (trials) took place, consisting of a 2-minute period of exposure to infrared radiation (with the laser being switched on, hence referred to as the ON period) and a subsequent resting period of 4 minutes (laser being switched off, referred to as the OFF period). The supply current of the laser was set to 400 mA DC in the ON state, which resulted in a temperature elevation of 2.4 °C.

2.6   Analysis of in vivo electrophysiological data

2.6.1 Evaluation of the signal-to-noise ratio

To assess the capability of the optrode in carrying out extracellular recordings in vivo, the signal-to-noise ratio (SNR) was determined for every channel. The method applied to calculate the SNR [Fiáth, 2021] is based on the observation that during the down-states of ketamine-xylazine-induced cortical slow-wave activity, most cortical neurons stop firing for a few hundred milliseconds [Fiáth, 2016] (see Supplementary Figure S4). These brief time windows allow for an estimation of the recording's noise level from the multiunit activity (MUA). During up-states, cortical neurons display high spiking activity, which thus can be utilized to estimate the signal level. Therefore, the ratio of MUA during up-states (high spiking activity) to down-states (low spiking activity) provides a relatively accurate estimation of SNR of the recording.

To calculate the SNR, first a bandpass filter (500-5000 Hz) was applied on the continuous wideband recording, followed by rectification of the filtered signal, to extract MUA. Next, this bandpass filtered signal underwent smoothing using a moving average with a window size of 10 ms. In the subsequent step, the onset of up- and down-states were determined through thresholding. The average value of the smoothed signal served as the threshold. Signal points that exceeded this value were classified as being part of an up-state. However, thresholding leads to minor gaps in the "true" up-states. To bridge these gaps, a data point is identified as an up-state if another up-state point is present within 50 ms. Afterwards, up- and down-states lasting over 200 ms are selected to establish the actual up- and down-states, which are usually several hundred milliseconds long. This minimum duration criterion is necessary to eliminate falsely detected states identified by the algorithm. To avoid utilizing the transitional zones between up- and down-states, a 150 ms duration at the midpoint of these selected states is used for the next step. Root mean square (RMS) values were determined for the selected intervals in both the up- and down-states. The SNR is determined by dividing the average RMS value of the up-states by the average RMS value of the down-states.

2.6.2 Analysis of the optrode recordings

We also investigated the effect of infrared neuromodulation on neuronal spiking rates. To achieve this, single and multi unit activity was extracted from the recorded extracellular data utilizing the Kilosort 2.0 automatic spike sorting algorithm [Pachitariu, 2016]. The output of Kilosort underwent manual curation using the open source Phy library [Phy, 2023], improving the result of the automatic spike

sorting algorithm through human judgement. Through manual curation, the clusters detected by Kilosort were merged or split, and noise clusters were eliminated. The remaining clusters were classified as either SUA or MUA clusters. A cluster was qualified as MUA if the shape of the spike waveform was atypical (including clusters with very low amplitude spike waveforms or clusters containing several different spike waveforms which could not be split) or if no clear refractory period was present in the auto-correlogram.

For each SUA or MUA cluster, we calculated the relative firing rate in non-overlapping ten-second intervals for each ON period, as illustrated in the following equation:

$$Relative\ firing\ rate\ =\ \frac{Firing\ rate - Baseline}{Baseline} \qquad (3)$$

The baseline was defined as the average firing rate during the last two minutes of the OFF periods preceding the ON periods, while the firing rate was defined as the average firing rate of the neuron during the ten-second-long interval. To examine the correlation between the IR stimulation and the firing rate change of SUA and MUA clusters, the following classification was performed. Neuron clusters activated (suppressed) by IR stimulation had to display a firing rate increase (decrease) by at least 20% compared to their baseline firing rate during at least 60% of the ON periods.

2.6.3 Comparison of the neuromodulation effect between neocortical locations

To compare differences in the extent of neuromodulation achieved with the mirror-tip optrode at different cortical locations, we analyzed high-density electrophysiological data recorded either close (n = 4 recordings) or further away (n = 3) from the theoretical focal point of infrared irradiation (Figure 7A). To examine changes in the level of neuronal population activity (MUA), we first detected the onset of up-states similarly as described above (see section 2.6.1). Briefly, the original electrophysiological signal (Neuropixels recording) was bandpass filtered (500 – 5000 Hz, zero-phase shift) and rectified to obtain the MUA. The MUA was then summed up across all channels located in the neocortex and smoothed with a low-pass filter (third-order Butterworth filter, 50 Hz, zero-phase shift). Next, to determine the onset of up- and down-states, we calculated an amplitude threshold from the smoothed MUA based on MUA values during down-states (no activity). The onset of an up-state was defined as the time point when the amplitude value of the SPA signal exceeded the calculated threshold level. Next, of the detected up-states, we removed those with very long and short durations, which are often the result of incorrect or inaccurate state detections. To calculate MUA averages both for the stimulation (ON) and the baseline (OFF) periods, short snippets were cut from the continuous MUA recordings around the detected up-state onsets (150 ms before and 300 ms after the onset), then, for each stimulation trial, these snippets were averaged across up-states and cortical channels. Only up-states detected during the second minute of the two-minute-long ON periods (95 ± 15 up-states per stimulation trial; mean ± SD) and the last minute of the four-minute-long OFF periods (92 ± 18 up states per trial) were used to compute the MUA averages. Figure 7B shows the average cortical MUA in one of the rats during ON and OFF periods (MUA was averaged across the ten stimulation trials). Finally, for both cortical locations (anterior and posterior to the optrode, termed as "front" and "behind", respectively), we calculated the change in the MUA level during stimulation (ON) relative to the baseline (OFF) period within a 50-ms-long time window (Figure 7B, shaded region), starting 10 ms after the up-state onset (Figure 7C). To examine changes in the low frequency range corresponding to cortical slow-wave or delta activity, we computed the power spectrum (Fast Fourier transform, FFT) on each cortical channel, in the same time interval as described above for the MUA (second minute of stimulation and fourth minute of the baseline period). For each stimulation trial, the power spectrum was then averaged across channels. Figure 7D shows the average spectra between 0.8 and 10 Hz in one of the rats during ON and OFF periods (spectra were averaged across the ten stimulation trials).

Finally, at both cortical locations, we calculated the change in the power in the delta frequency band (1-4 Hz; Figure 7D, shaded region) during stimulation relative to the baseline period (Figure 7E).

2.7   Histology

To detect the tracks of the optrode and the Neuropixels probe in the brain tissue, we used a histological procedure described previously [Fiáth, 2016; Fiáth, 2019]. In short, the rats were deeply anaesthetized after collecting the neural data, then they were transcardially perfused with physiological saline solution (100 ml) followed by a fixative solution containing 4% paraformaldehyde in 0.1 M phosphate buffer (PB; pH=7.4, 250 ml). The fixed brain was stored at 4 °C overnight.

For the experiments with electrophysiology (n = 4 rats), the brain tissue was processed by first cutting 60-μm-thick coronal sections with a vibratome (Leica VT1200, Leica Microsystems, Wetzlar, Germany). Following washing in 0.1 M PB, brain sections were placed first in a Petri dish containing gelatin, then they were mounted onto microscopic slides and air dried. To identify brain sections containing fluorescent marks of DiI corresponding to the Neuropixels probe track, the slides were examined under a light microscope (Leica DM2500, Leica Microsystems) equipped with a fluorescence LED illumination source (SFL4000, Leica) and with a digital camera (DP73, Olympus, Tokyo, Japan). The track of optrode could be clearly identified in the brain sections without using DiI because of its larger shank cross-sectional area. After that, the brain sections were processed for cresyl violet (Nissl) staining, dehydrated in xylene and cover-slipped with DePex (SERVA Electrophoresis, Heidelberg, Germany). Finally, Nissl-stained sections containing the optrode and Neuropixels probe tracks were photographed under the microscope.

For the experiment designed for histological evaluation of the IR stimulation safety (n = 1 rat), the samples were cut into 60-μm-thick horizontal sections with the vibratome after fixation. The samples were then immersed in 30% sucrose for 1 day. Next, the slices were frozen above liquid nitrogen three times. After that, to visualize neurons, the slices were immunostained against Neuronal Nuclei (NeuN, Millipore, clone A60, 1:2000). The samples were then transferred into 0.1 M PB and washed 3 times for 10 minutes. All the following steps of the immunostaining protocol were carried out in 0.1 M PB. The endogenous peroxidase was blocked by 1% H_2O_2 for 10 minutes. After a 10-minute-long wash, the aspecific staining was blocked by 2% Normal Goat Serum and 2% Normal Horse Serum for 1 hour. After a 5-minute-long wash, we applied the primary antibody for 3 days at 4 °C. After 3 washes, biotinylated anti-mouse IgG (1:250, Vector, Burlingame, CA, USA) were applied for 2 hours, followed by avidin-biotinylated horseradish peroxidase complex (ABC, 1:250, 1.5 h, Vector, Burlingame, CA, USA) for visualizing the staining. After subsequent washes, the immune peroxidase reaction was developed with 1% 3,3-diaminobenzidine tetrahydrochloride. The slices were then dehydrated in two steps in xylene for 10 minutes and mounted with DePex into microscope slides.

Optical microscopy images were acquired by a Slide Scanner (Pannoramic MIDI II, 3DHISTECH) in 20-fold magnification, and exported at 300 dpi in TIFF file format.

2.8   Image processing

Neuronal cell loss was quantified using the NeuN stained slices in regions of interests (ROIs) outlined between the center of the track and 300 μm from that in 50 μm step sizes (see Figure 8E for more detailed explanation). Neuronal nuclei were counted manually in each ROI using the Case Viewer (3DHISTECH) software. Neuronal cell density was counted in each ROI and values were normalized to the value in the outermost region used as control (between 250-300 μm from the probe track). Since the normalized cell density values for both sham-stimulated (control) and IR stimulated tracks were found to be of normal distribution, we used Student's paired t-test to evaluate differences.

3   Results

3.1   Electrochemical characterization

To improve the quality of neuronal recordings, electroplated platinum was deposited on top of the sputtered platinum recording sites. Figure 2 shows the results of the electrochemical characterization of the recording sites before (Figure 2A-B) and after (Figure 2C-D) the deposition of porous platinum in case of a representative optrode device. In view of the Bode plots, it was noticed that site impedance was successfully reduced. The average of the absolute value of impedance decreased from an initial value of 4.09 ± 1 MΩ to 323 ± 68.3 kΩ (n = 15 sites) at 1 kHz during the electrochemical process. This final value makes the device suitable to capture single unit activity in the brain tissue. Supplementary Fig. S5 shows the result of a 7-day-long soaking test. The magnitude (A) and phase (B) of the impedance at 1 kHz was measured twice a day for each 16 recording sites. Each point on the curves represents the average of all 16 sites. The individual trials are distinguished by the letters a and b. The lack of any adverse trend in impedance change gives evidence on the stability of electrophysiological sensors.
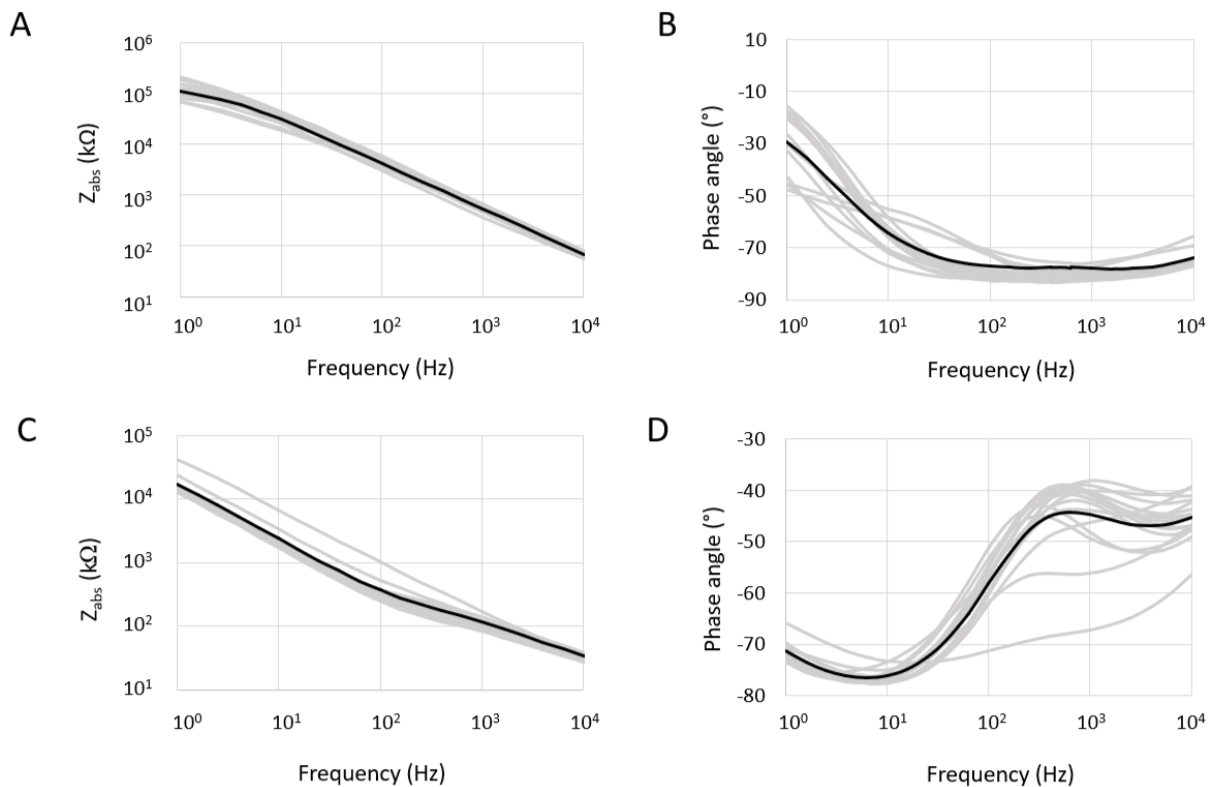
Figure 2. Bode plots derived from the electrochemical characterization of a representative optrode device. Magnitude (A) and phase diagram (B) of the sputter deposited recording sites. Magnitude (C) and phase (D) diagram of the characterized recording sites after electroplating. Grey and black curves represent the plots of individual sites (n=15) and the average values across the frequency range, respectively.

3.2   Heat-distribution around the micromirror optrode tip

During the characterization of the temperature distribution around the mirror-tip probe end, we exploited the dataset measured on previously used blunt-tip and sharp tip probe profiles as controls (Figure 3A). The temperature change at various supply current values used for the IR illumination with a representative optrode device is illustrated on Figure 3B [Horváth, 2020; Horváth, 2022]. The linear relationship is in line with our expectations already experienced during the use of optrodes with other

tip profiles. Besides, the axial and perpendicular heat profile in the close vicinity of the probe tip exhibits remarkable and beneficial differences with respect to the reference devices (dotted line and dashed line in Figure 3C & D), for which data have been previously published [Horváth, 2020; Horváth, 2022]. The maximum temperature gets closer to the probe tip in the X axis, while a shift exceeding 200 µm in the Y direction highlights the asymmetric temperature profile achieved by the integrated parabolic micromirror.
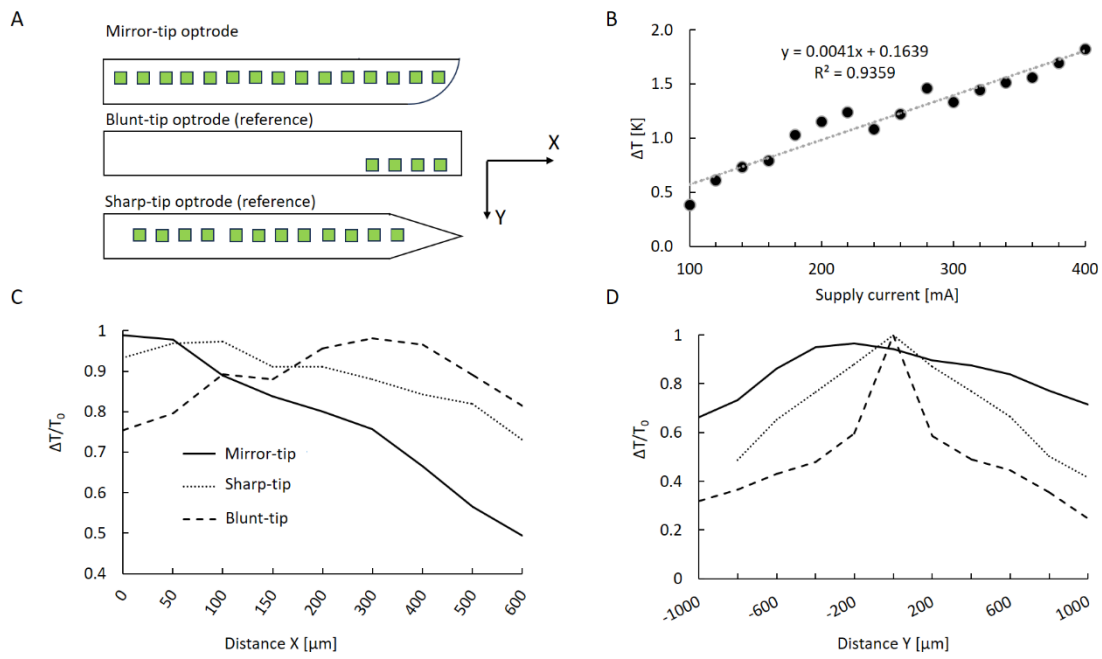
Figure 3. Characterization of the temperature increase induced by the optrode. (A) Definition of directions to characterize heat distributions. The blunt-tip and sharp-tip optrodes are also added as a reference device. (B) Calibration curve (temperature vs. supply current of the laser diode) of a representative mirror-tip optrode at coordinates x = 200 µm, y = 0. Equation of the fitted linear curve and goodness of fit are denoted. (C) Decay of temperature along the X axis from the tip of the probes (x = 0; y = 0). (D) Decay of the temperature along the Y axis at the coordinate x = 200 µm. The curves of the micromirror tip optrode drawn as a solid line on panels C & D show the averaged results of experiments repeated twice on all 4 individual optrode devices tested. The dotted and dashed curves are previously published data, redrawn here for the sake of comparison [Horváth, 2022].

3.3 Electrophysiological recordings

The results of the electrophysiological characterization of the mirror-tip optrode are illustrated in Figure 4. Figure 4A & B depicts a representative wideband and high-pass filtered signal (MUA) of a single optrode recording channel, respectively. Figure 4 C&D shows the average SNR of a 60-minute-long optrode measurement along nine consecutive stimulus trials. It is visible that the SNR does not change significantly during ON periods (1.89±0.46; mean ± SD; Figure 4C) and OFF periods (1.83±0.42; Figure 4D), which proves that the device is not sensitive to the potential light-induced artifacts during IR stimuli. Furthermore, the stimulus onset does not alter the signal quality on individual recordings sites located along the probe shaft (see Figure 4E).
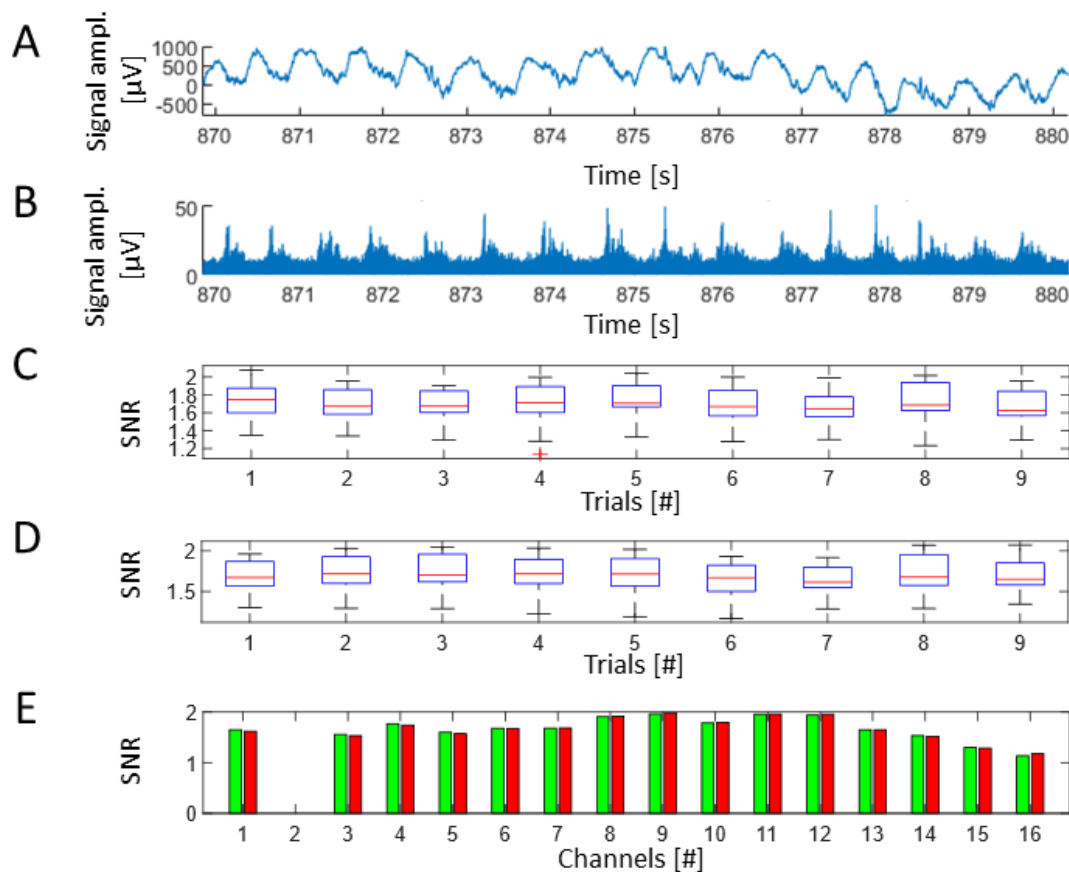
Figure 4. Signal quality during electrophysiological recordings. Representative wideband (A) *and high-pass filtered (B) cortical activity recorded on an optrode channel. (B) Average signal-to-noise ratio (SNR) calculated during consecutive stimulation (ON) periods. (C) Average* SNR *calculated during consecutive OFF periods. (D)* SNR *of individual channels of an optrode measured during nine consecutive stimulus trials, green and red bars show values calculated during ON and OFF periods, respectively.*

The firing rates of single unit and multiunit clusters were visualised as shown in Figure 5. The timing of the infrared stimulation is depicted by red vertical lines on the graphs. Figure 5A qualitatively represents how the firing rate changes over time within a cluster (intra-cluster firing rate). The firing rate for each neuron cluster was normalised over time. Brighter yellow regions indicate a higher firing rate, while darker blue regions correspond to a lower firing rate. This graph provides an overview of cluster response to IR irradiation, indicating whether the optical stimulation protocol affects all clusters or only a smaller subset. However, it is not appropriate for making quantitative comparisons of firing rates among different clusters. On Figure 5B and C, two representative single units that were suppressed and activated during IR stimulation are shown along ten consecutive trials. The evoked responses were mostly stable and robust and did not reveal any signs of irreversible changes on the firing activity of the interrogated units.
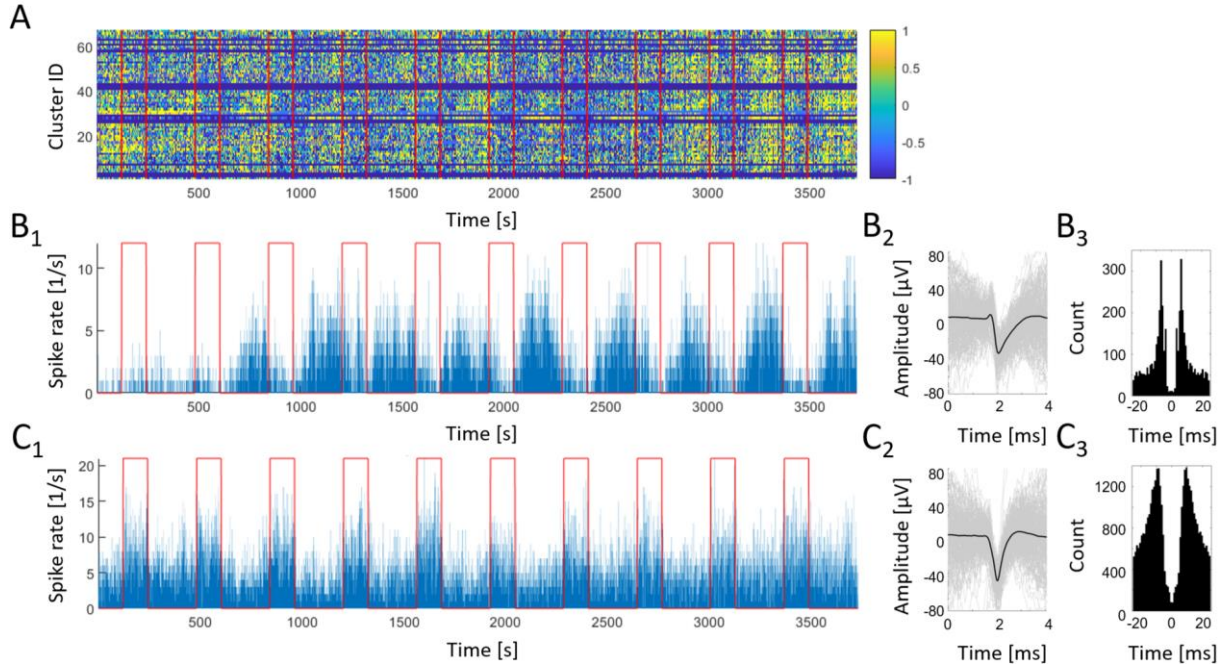
Figure 5. Effect of infrared irradiation on single- and multiunit activity. (A) Normalized firing rate changes within individual single- and multi-units over ten consecutive IR stimulus. The brighter yellow regions reflect a higher firing rate, while darker blue regions indicate a lower firing rate. All units are from a single rat. (B₁) Firing rate change over time, (B₂) spike waveforms and (B₃) auto-correlogram of an example single unit selected from the 60 units shown in panel (A). The activity of the neuron was suppressed upon stimulation. (C₁) Firing rate change over time, (C₂) spike waveforms and (C₃) auto-correlogram of another single unit during the IR stimulation session. The neuron responded with an increased firing rate upon stimulation. Periods denoted with red frames in panels (A), (B₁) and (C₁) refer to the onset and offset of IR stimulation, and each blue column in panels (B₁) and (C₁) represents the spike rate within a 1-second-long timeframe. The black curve in panels (B₂) and C₂) is the average of 200 individual spikes (grey lines).

The number of clusters isolated during spike sorting of electrophysiological signals derived from the acute in vivo experiments described above is summarized in Table 1, along with the number of neurons responding with increased or suppressed activity to stimulation.

Experiment	SUA	MUA	Activated neurons		Suppressed neurons	
			SUA	MUA	SUA	MUA
#1	27	102	1	2	9	13
#2	35	107	2	1	6	5
#3	12	89	0	0	2	0
#4	29	102	2	7	3	3

Table 1. Results of the spike sorting process. Each row represents a separate experiment in which extracellular neural activity was recorded from a rat. The second and third columns show the number of clusters classified as single unit (SUA) or multi unit (MUA) clusters. The subsequent columns illustrate the number of SUA and MUA clusters exhibiting markedly increased or decreased firing rates during IR irradiation (ON period), respectively (i.e., neurons activated and suppressed by stimulation).

Figure 6 displays the relative firing rate changes of a single unit compared to the relative temperature changes (i.e. heating) during five consecutive ON and OFF periods. Following the increase in temperature, the firing rate decreases and reaches its minimum value during the saturation of temperature. When the stimulation phase is finished, we can observe the gradual recovery of both the firing rate and the temperature to the original regime.
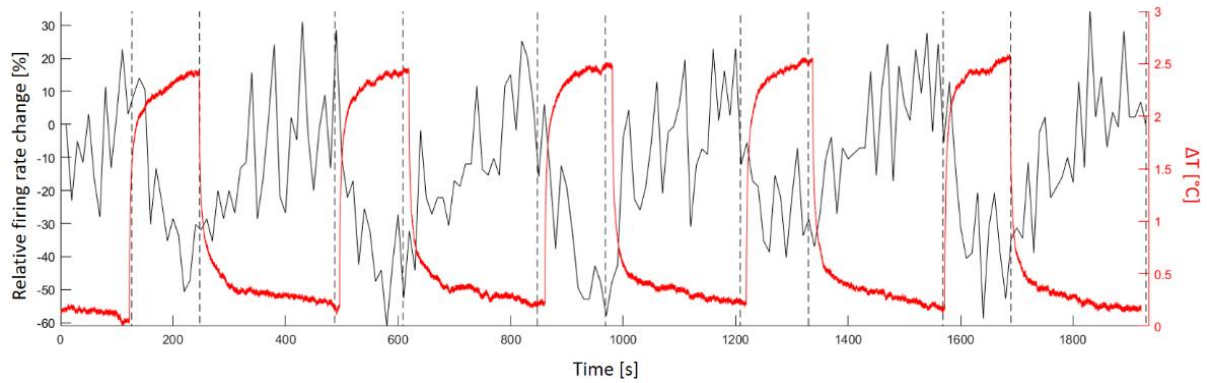

Figure 6. Relative change of the firing rate of a representative single unit recorded by one of the sites of the micromirror tip optrode during IR stimulation protocol (black curve, primary vertical axis). The firing rate was calculated in non-overlapping 10-second-long time windows, then compared to the baseline period (last two minutes of OFF periods preceding the stimulation). Relative temperature change measured under bench-top circumstances (red curve, secondary vertical axis) from an IR protocol that is identical in all its parameters. The mutual position of the two probes during temperature measurement was (x;y)=(100;0)[µm].

We hypothesized that the asymmetric temperature profile of the mirror-tip optrode implies that the extent of neuromodulation will be also different in front of and behind the micromirror. To test this assumption, we aligned a Neuropixels probe in these two positions (see Figure 7A) and recorded the response of the affected neuronal population. Both the up-state-related multiunit activity and the power in the delta frequency band (1-4 Hz) was significantly higher during infrared stimulation compared to the subsequent control period (MUA, ON vs. OFF period, 7.03 ± 1.50 au vs. 6.43 ± 1.44 au, Wilcoxon signed rank test, $Z = 6.931$, $p < 0.001$, Figure 7B; delta band, ON vs. OFF period, 16.90 ± 5.92 au vs. 15.94 ± 5.52 au, Wilcoxon signed rank test, $Z = 6.528$, $p < 0.001$, Figure 7D). The increase in these metrics was also significantly larger for recordings obtained with the probe located closer to the focal point of the micromirror (MUA, "front" vs. "behind", 12.30 ± 9.58 % vs. 6.30 ± 5.51 %, Mann-Whitney U test, $Z = 2.558$, $p = 0.0105$, Figure 7C; delta activity, "front" vs. "behind", 7.14 ± 6.64 % vs. 3.32 ± 4.61 %, Mann-Whitney U test, $Z = 2.534$, $p = 0.0113$, Figure 7E), proving the feasibility of the new illumination concept.
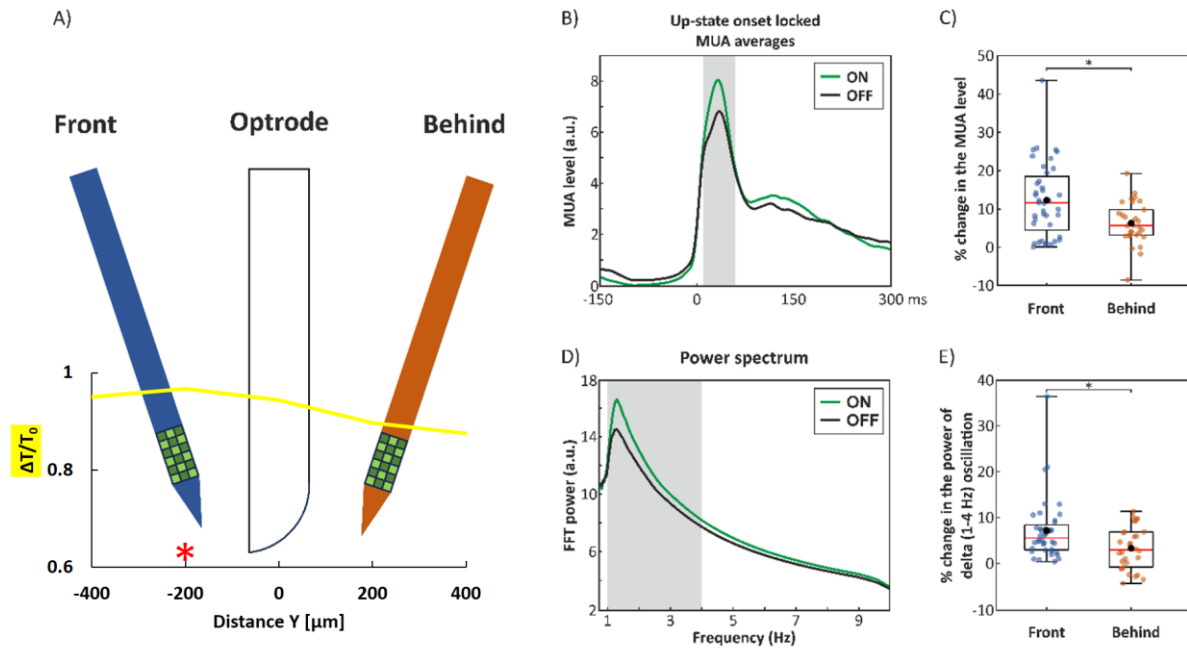
*Figure 7. Neural recordings demonstrating the effect of the asymmetric outcoupling profile on the activation of neurons. (A) Schematics on the approximate location of the optrode relative to the recording probe. The micromirror tip optrode was implanted perpendicularly to the cortical surface at 2 mm depth, while the Neuropixels probe was implanted at a degree of 25° from vertical to a depth of approximately 3 mm. In each experiment, during the first measurement, the probe was located about 300 μm anterior from the optrode ("Front"), while for the second recording, it was inserted approximately 300 μm posterior from the optrode ("Behind"). Inset curve drawn in yellow shows a section of the spatial distribution of the optically induced heating along axis Y perpendicular to the optrode shaft. The place of maximum of optically induced heating along the micromirror tip is marked with a red asterisk (cf. Fig. 3. C&D). (B) Average cortical multiunit activity (MUA) locked to the onset of up-states during infrared stimulation (green, ON) and baseline activity (black, OFF). The up-state starts at time point zero. The MUA was obtained from a single rat and was averaged across cortical layers and stimulation trials. (C) Change in the MUA level during stimulation trials relative to the baseline activity for recordings obtained with the probe located in front of (blue; n = 40 trials from 4 rats) or behind (red; n= 30 trials from 3 rats) the optrode. The values were computed by averaging the MUA in a 50-ms-long time window (shaded region in panel B). The features of boxplots are as follows. The line in the middle of the box represents the median, whereas the edges of box mark the 25th and 75th percentiles. Whiskers indicate the minimum and maximum values, while the black dot represents the average value. Individual values are indicated with colored dots. (D) Representative power spectrum of cortical recording during infrared stimulation (green) and baseline activity (black). Spectra were computed from the recording of a single rat and were averaged across stimulation trials. (E) Change in the power in the delta frequency band (1-4 Hz; shaded region in panel D) during stimulation relative to the baseline activity for recordings obtained with the probe located in front of (blue; n = 40 trials from 4 rats) or behind (red; n = 30 trials from 3 rats) of the optrode. The features of boxplots are the same as in panel C. For panels B-E, neural activity in the last minute of the ON period (stimulation) was compared to the last minute of the OFF period (baseline). * p < 0.05.*

3.4   Histological evaluation

The tip of the optrode is designed to finetune the light profile and shift the location of the stimulated region very close to the recording sites. On the first hand, it is reasonable to confirm the safety of the

neuromodulation approach using this device and compare the results with our previous findings coming from the evaluation of blunt and sharp tip IR optrode devices [Horvath, 2022]. On the other hand, we have a unique opportunity to observe the combined effect of the implantation and IR irradiation, since they can be analyzed by histological examination of tissue slices containing both the track and the directly stimulated region at the same time. Figure 8 summarizes the evaluation of NeuN-stained slices covering the cortical region where the mirror-tip was located. The neuronal density was analyzed in five neighboring slices located 60 µm from each other in different cortical depths. Picture of a typical NeuN-stained slice is shown for both sham-stimulated (control, Figure 8A) and IR stimulated regions (Figure 8B). Location and specific areas covered by the applied ROIs around the probe track are shown in Figure 8E. Since cell density changes across the implantation depth, this value is normalized to the value derived from ROI 6. Figure 8C and D represent the change of normalized cell densities for the control region and IR stimulated region, respectively. Figure 8F compares the normalized cell density values from all control (n = 2) and stimulated (n = 2) tracks and slices (five slices for each). Based on a paired t-test (p < 0.05), we found no statistically significant difference between neuronal density measured in control and stimulated case within the same ROIs (p_{ROI1} = 0.492032, p_{ROI2} = 0.088713, p_{ROI3} = 0.411541, p_{ROI4} = 0.200894, p_{ROI5} = 0.478253).
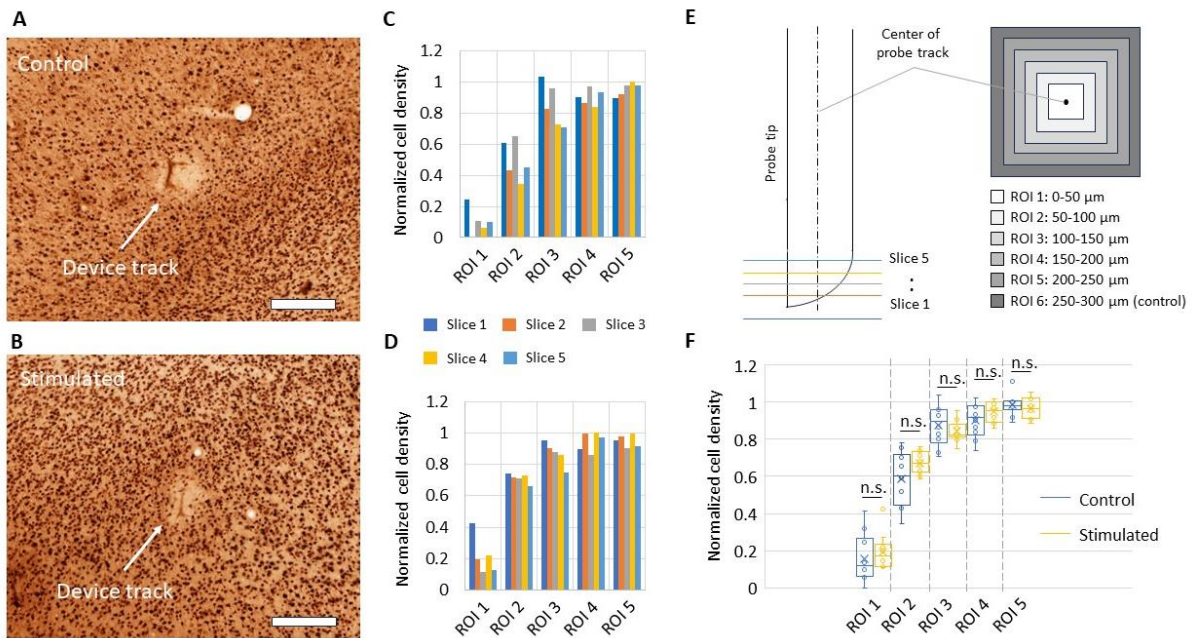

Figure 8. Histology results. A) Representative NeuN-stained slice around the sham-stimulated (control) tissue. B) Representative NeuN-stained slice around IR stimulated region. Both A) and B) shows a picture of slice 3 located in a depth of 180 µm from the device tip. Scale bar represents 100 µm. C) and D) shows the normalized cell density counted across each slice in different region of interests (ROIs) around two selected probe tracks in the case of control and stimulated tissue, respectively. E) Explanation of the location of slices and ROIs. F) Comparison of normalized cell densities around control and stimulated tissue (n = 10 for each ROI and condition).

4   Discussion

This study proposed a new intracortical multimodal optrode designed for infrared stimulation that provided a lateral outcoupling profile, and therefore positioning the directly irradiated and heated tissue volume closer to the integrated recording sites of the device. The novel concept makes it

possible to measure thermally evoked potentials by interrogating irradiated neurons directly. In our experiments, performance of the mirror-tip device is benchmarked against previous layouts (blunt and sharp tip optrodes) reported by our group [Horvath, 2020; Horvath, 2022]. The efficacy of the integrated parabolic micromirror at the probe tip to relocate the temperature maximum around the device track was successfully demonstrated. This property is especially useful for experimental conditions, where specific cortical layers or population of cells are targeted, while simultaneous extracellular recording in the stimulated region is needed. Besides the transmission of IR light into the tissue, our device was able to measure the action potentials of single neurons with adequate signal-to-noise ratio, which is essential to characterize IR-induced neuromodulation within the cortex in the future. An important highlight of the present design is that it proved the feasibility of shaping photonic components on silicon-based neural optrodes to tailor the irradiation profile in the tissue. Besides the modulation of the lateral position of the heat profile, the temperature maximum in the current design is also getting closer to the recording sites located on the probe shaft, which provides further advantage to evaluate the thermally evoked response of the irradiated tissue. Compared to the recently published optrode devices for infrared stimulation [Meneghetti, 2023; Wan, 2021], our unique micromachining approach may open new pathways to construct implantable microdevices intended to monitor the response of individual neurons upon IR exposure with high spatial precision. A further advantage of the concept is that our technology is fully customizable [Kiss, 2016], facilitating to reach of deep tissue structures in various animal models. Furthermore, due to the adherence to a MEMS fabrication scheme, low variability between individual optrode devices can be guaranteed, which helps to record statistically meaningful data, while reducing animal subjects. Biocompatibility is also a key issue in the field of infrared neuromodulation [Chernov, 2014; Horvath, 2022]. Regarding histological data, we can say that stimulating through integrated micromirror can be safely performed without apparent loss in the cell density compared to sham-stimulated cases. Overall, our dataset on the thermal, electrophysiological and histological characterization reported in this paper highlights the efficient operational capabilities of the proposed technology, which is mature enough to transfer into chronic experimental conditions in the near future.

5 Acknowledgement

6 Conflict of interest

The authors declare no conflict of interest.

7 References

Abaya, T. V. F., Diwekar, M., Blair, S., Tathireddy, P., Rieth, L., Clark, G. A., & Solzbacher, F. (2012). Characterization of a 3D optrode array for infrared neural stimulation. *Biomedical optics express*, *3*(9), 2200-2219.

Boros, Ö. C., Horváth, Á. C., Beleznai, S., Sepsi, Ö., Csősz, D., Fekete, Z., & Koppa, P. (2019). Optimization of an optrode microdevice for infrared neural stimulation. *Applied Optics*, *58*(14), 3870-3876.

Chernov, M., & Roe, A. W. (2014). Infrared neural stimulation: a new stimulation tool for central nervous system applications. *Neurophotonics*, *1*(1), 011011-011011.

Fan, B., & Li, W. (2015). Miniaturized optogenetic neural implants: a review. *Lab on a Chip*, 15(19), 3838-3855.

Fekete, Z. (2015). Recent advances in silicon-based neural microelectrodes and microsystems: a review. *Sensors and Actuators B: Chemical*, *215*, 300-315.

Fekete, Z., Csernai, M., Kocsis, K., Horváth, Á. C., Pongrácz, A., & Barthó, P. (2017). Simultaneous in vivo recording of local brain temperature and electrophysiological signals with a novel neural probe. *Journal of Neural Engineering*, *14*(3), 034001.

Fekete, Z., Horváth, Á. C., & Zátonyi, A. (2020). Infrared neuromodulation: a neuroengineering perspective. *Journal of Neural Engineering*, *17*(5), 051003.

Fiáth et al. Slow insertion of silicon probes improves the quality of acute neuronal recordings. (2019) Scientific reports 9 (1), 1-17.

Fiath, R., Kerekes, B.P., Wittner, L., Toth, K., Beregszaszi, P., Horvath, D., Ulbert, I., 2016. Laminar analysis of the slow wave activity in the somatosensory cortex of anesthetized rats. Eur J Neurosci 44, 1935-1951. 10.1111/ejn.13274.

R. Fiáth, D. Meszéna, Z. Somogyvári, et al., "Recording site placement on planar silicon-based probes affects signal quality in acute neuronal recordings," Scientific Reports, vol. 11, no. 1, Jan. 2021. doi: 10.1038/s41598-021-81127-5. [Online]. Available: https://doi.org/10.1038/s41598-021-81127-5.

Horváth, Á. C., Boros, Ö. C., Beleznai, S., Sepsi, Ö., Koppa, P., & Fekete, Z. (2018). A multimodal microtool for spatially controlled infrared neural stimulation in the deep brain tissue. *Sensors and Actuators B: Chemical*, *263*, 77-86.

Horváth, Á. C., Borbély, S., Boros, Ö. C., Komáromi, L., Koppa, P., Barthó, P., & Fekete, Z. (2020). Infrared neural stimulation and inhibition using an implantable silicon photonic microdevice. *Microsystems & nanoengineering*, *6*(1), 44.

Horváth, Á. C., Borbély, S., Mihók, F., Fürjes, P., Barthó, P., & Fekete, Z. (2022). Histological and electrophysiological evidence on the safe operation of a sharp-tip multimodal optrode during infrared neuromodulation of the rat cortex. *Scientific Reports*, *12*(1), 11434.

Horvath, C., Ulbert, I., & Fiath, R. (2023). Propagating population activity patterns during spontaneous slow waves in the thalamus of rodents. *NeuroImage*, 120484

Kampasi, K., English, D. F., Seymour, J., Stark, E., McKenzie, S., Vöröslakos, M., ... & Yoon, E. (2018). Dual color optogenetic control of neural populations using low-noise, multishank optoelectrodes. *Microsystems & nanoengineering*, *4*(1), 10.

Kim, K., Vöröslakos, M., Seymour, J. P., Wise, K. D., Buzsáki, G., & Yoon, E. (2020). Artifact-free and high-temporal-resolution in vivo opto-electrophysiology with microLED optoelectrodes. *Nature communications*, *11*(1), 2063.

Kiss, M., Földesy, P., & Fekete, Z. (2016). Optimization of a Michigan-type silicon microprobe for infrared neural stimulation. *Sensors and Actuators B: Chemical*, *224*, 676-682.

Kozai, T. D. Y., Du, Z., Gugel, Z. V., Smith, M. A., Chase, S. M., and Bodily, L. M. (2015). Comprehensive chronic laminar single-unit, multi-unit, and local field potential recording performance with planar single shank electrode arrays. *J. Neurosci. Methods* 242, 15–40. doi: 10.1016/j.jneumeth.2014.12.010

Lanzio, V., Telian, G., Koshelev, A., Micheletti, P., Presti, G., D'Arpa, E., ... & Cabrini, S. (2021). Small footprint optoelectrodes using ring resonators for passive light localization. *Microsystems & nanoengineering*, *7*(1), 40.

Li, L., Lu, L., Ren, Y., Tang, G., Zhao, Y., Cai, X., ... & Sheng, X. (2022). Colocalized, bidirectional optogenetic modulations in freely behaving mice with a wireless dual-color optoelectronic probe. *Nature Communications*, *13*(1), 839.

Márton, G., Bakos, I., Fekete, Z., Ulbert, I., and Pongrácz, A. (2014). Durability of high surface area platinum deposits on microelectrode arrays for acute neural recordings. *J. Mater. Sci. Mater.* Med. 25, 931–940. doi: 10.1007/s10856-013-5114-z

Marcello Meneghetti, Jaspreet Kaur, Kunyang Sui, Jakob F. Sørensen, Rune W. Berg, Christos Markos (2023). Soft monolithic infrared neural interface for simultaneous neurostimulation and electrophysiology. *Light Sci Appl 12*, 127, doi: 10.1038/s41377-023-01164-9

McAlinden, N., Cheng, Y., Scharf, R., Xie, E., Gu, E., Reiche, C. F., ... & Mathieson, K. (2019). Multisite microLED optrode array for neural interfacing. *Neurophotonics*, *6*(3), 035010-035010.

Mohanty, A., Li, Q., Tadayon, M. A., Roberts, S. P., Bhatt, G. R., Shim, E., ... & Lipson, M. (2020). Reconfigurable nanophotonic silicon probes for sub-millisecond deep-brain optical stimulation. *Nature biomedical engineering*, *4*(2), 223-231.

Pachitariu, M., Steinmetz, N., Kadir, S., Carandini, M., & Kilosort, H. K. D. (2016). realtime spike-sorting for extracellular electrophysiology with hundreds of channels. bioRxiv. *Preprint at*.

Paxinos, G. & Watson, C. The rat brain in stereotaxic coordinates. 6th edn, (Academic Press/Elsevier, 2007).

Phy 2023. [Online source]. Available: https://phy.readthedocs.io/en/latest/. Last visit: 06/12/2023

Reddy, J. W., Kimukin, I., Stewart, L. T., Ahmed, Z., Barth, A. L., Towe, E., & Chamanzar, M. (2019). High density, double-sided, flexible optoelectronic neural probes with embedded µLEDs. *Frontiers in Neuroscience*, *13*, 745.

Royer, S., Zemelman, B. V., Barbic, M., Losonczy, A., Buzsáki, G., & Magee, J. C. (2010). Multi-array silicon probes with integrated optical fibers: light-assisted perturbation and recording of local neural circuits in the behaving animal. *European Journal of Neuroscience*, *31*(12), 2279-2291.

Sacher, W. D., Chen, F. D., Moradi-Chameh, H., Luo, X., Fomenko, A., Shah, P., ... & Roukes, M. L. (2021). Implantable photonic neural probes for light-sheet fluorescence brain imaging. *Neurophotonics*, *8*(2), 025003.

Schwaerzle, M., Paul, O., & Ruther, P. (2017). Compact silicon-based optrode with integrated laser diode chips, SU-8 waveguides and platinum electrodes for optogenetic applications. *Journal of Micromechanics and Microengineering*, *27*(6), 065004.

Segev, E., Reimer, J., Moreaux, L. C., Fowler, T. M., Chi, D., Sacher, W. D., ... & Roukes, M. L. (2016). Patterned photostimulation via visible-wavelength photonic probes for deep brain optogenetics. *Neurophotonics*, *4*(1), 011002-011002.

Shim, E., Chen, Y., Masmanidis, S., & Li, M. (2016). Multisite silicon neural probes with integrated silicon nitride waveguides and gratings for optogenetic applications. *Scientific reports*, *6*(1), 22693.

Spagnolo, B., Balena, A., Peixoto, R. T., Pisanello, M., Sileo, L., Bianco, M., ... & Pisanello, F. (2022). Tapered fibertrodes for optoelectrical neural interfacing in small brain volumes with reduced artefacts. *Nature Materials*, *21*(7), 826-835.

Tian, H., Xu, K., Zou, L., & Fang, Y. (2022). Multimodal neural probes for combined optogenetics and electrophysiology. *Iscience*, *25*(1), 103612.

Wan, Y., Wang, M., Zhang, S., & Xie, B. (2021). Availability and safety assessment of infrared neural stimulation at high repetition rate through an implantable optrode. Journal of Innovative Optical Health Sciences, 14(03), 2150014.

Wu, F., Stark, E., Im, M., Cho, I. J., Yoon, E. S., Buzsáki, G., ... & Yoon, E. (2013). An implantable neural probe with monolithically integrated dielectric waveguide and recording electrodes for optogenetics applications. *Journal of neural engineering*, *10*(5), 056012.

Wu, F., Stark, E., Ku, P. C., Wise, K. D., Buzsáki, G., & Yoon, E. (2015). Monolithically integrated μLEDs on silicon neural probes for high-resolution optogenetic studies in behaving animals. *Neuron*, *88*(6), 1136-1148.

Yasunaga, H., Takeuchi, H., Mizuguchi, K., Nishikawa, A., Loesing, A., Ishikawa, M., ... & Sekiguchi, H. (2022). MicroLED neural probe for effective in vivo optogenetic stimulation. *Optics Express*, *30*(22), 40292-40305.

Yizhar, O., Fenno, L. E., Davidson, T. J., Mogri, M., & Deisseroth, K. (2011). Optogenetics in neural systems. *Neuron*, *71*(1), 9-34.
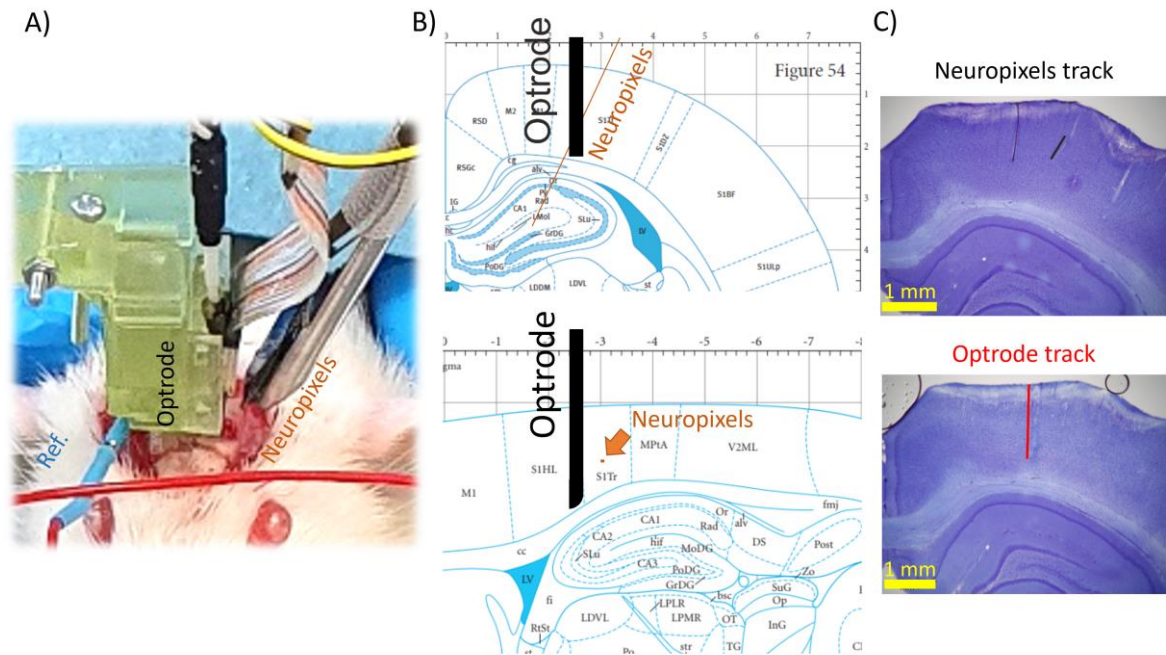
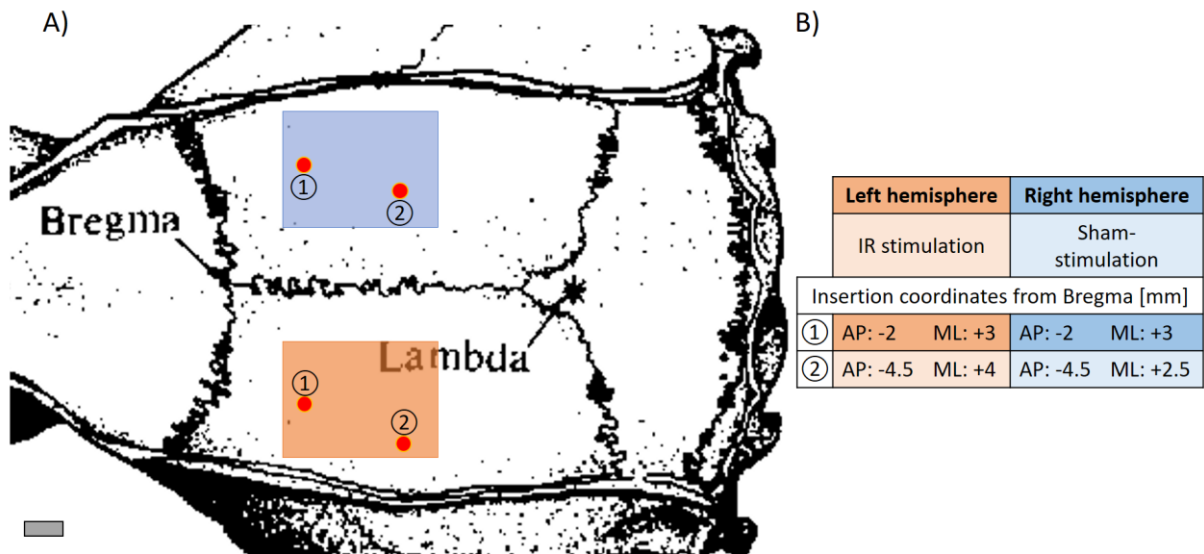# 8 Supplementary

Supplementary Figure S1
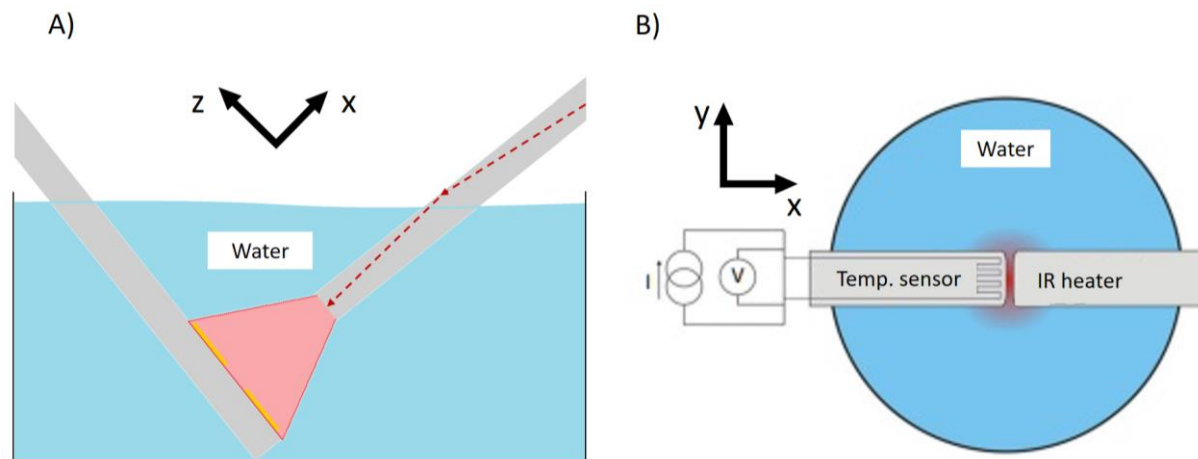
Supplementary Figure S1.: A) Side and B) top view of the bench-top optical heating measurement setup. Two thin needles, an IR waveguiding optrode (right) and a calibrated Pt temperature sensor integrated on the surface of a Si needle (left) are immersed in a polyethylene cylinder filled with ~2 ml water. Black arrows define the perpendicular axes X, Y, Z along which a series of temperature measurements were taken with 100 μm spatial resolution within ±1 mm range.
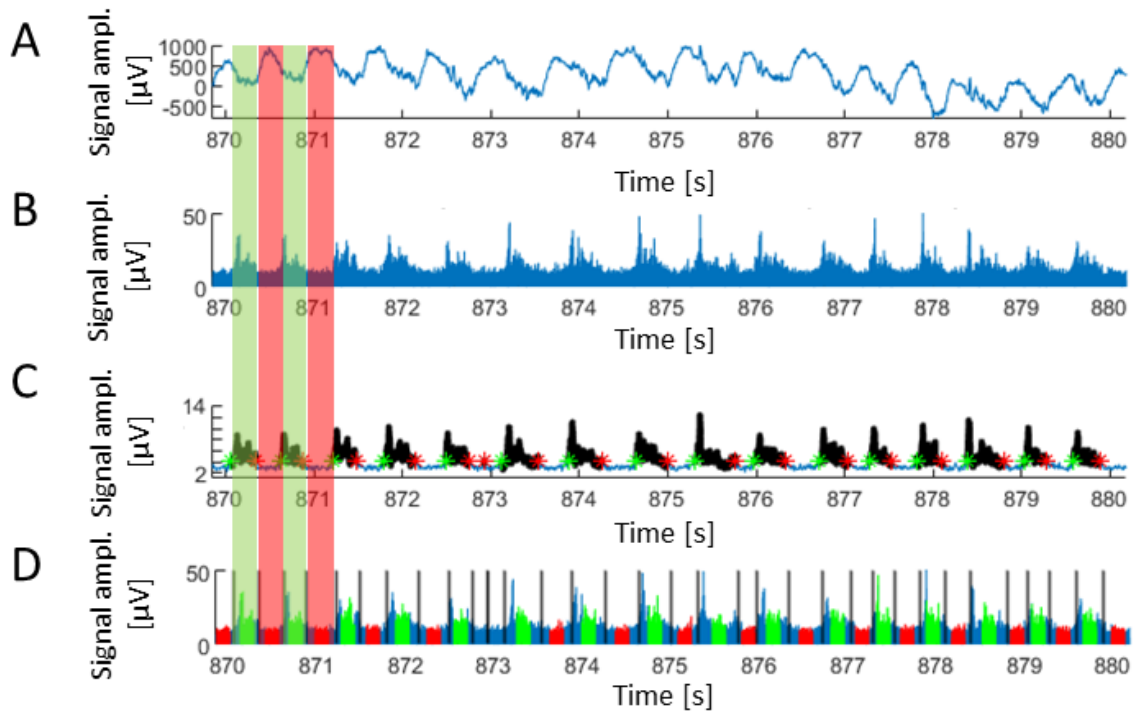
Supplementary Figure S2

Supplementary Figure S2.: A) Photo on in vivo surgical arrangement. B) Schematic illustrations of implantation drawn on coronal (top) and sagittal (bottom) schematic rat brain sections: IR optrode (black) was vertically implanted to reach 2 mm cortical depth; a Neuropixels 1.0 silicon probe (orange) was implanted at an angle of 25° and reached the hippocampus. Elements of the drawings are to scale: grid lines mark 1 mm. C) Nissl-stained coronal sections with implant track labels. Because the Neuropixels probe and the optrode were implanted at different locations along the anteroposterior axis separated by a distance of approximately 300 microns, their tracks are not visible on the same coronal section. Yellow scale bars on each subfigure on panel C show 1 mm.

Supplementary Figure S3

A)

B)

| Left hemisphere		Right hemisphere	
IR stimulation		Sham-stimulation	
Insertion coordinates from Bregma [mm]			
① AP: -2	ML: +3	AP: -2	ML: +3
② AP: -4.5	ML: +4	AP: -4.5	ML: +2.5

Supplementary Figure S3.: A) Explanatory drawing of the loci of craniotomies with marked implantation positions. Circled numbers and red spots indicate the location of the implantation tracks. Scale bar on the bottom left corner show 1 mm. B) Table lists the exact coordinates of each implantation.

Supplementary Figure S4. The steps of RMS-based signal-to-noise analysis. A) Raw signal (channel 6, 870-880 sec – 3rd ON period middle part). B) Bandpass filtered (500-5000 Hz) and rectified signal (MUA). C) Moving averaged data after bandpass filtering, green star: start of the up-state, red star: end of the up-state, black: points selected as up-state (above threshold) – (amplitude is smaller because of the moving averaging). D) Up- (green) and down-(red) state samples on the bandpass filtered signal, black vertical lines represent the borders of the states. Red shade: down-state, green shade: up-state.

Supplementary Figure S5
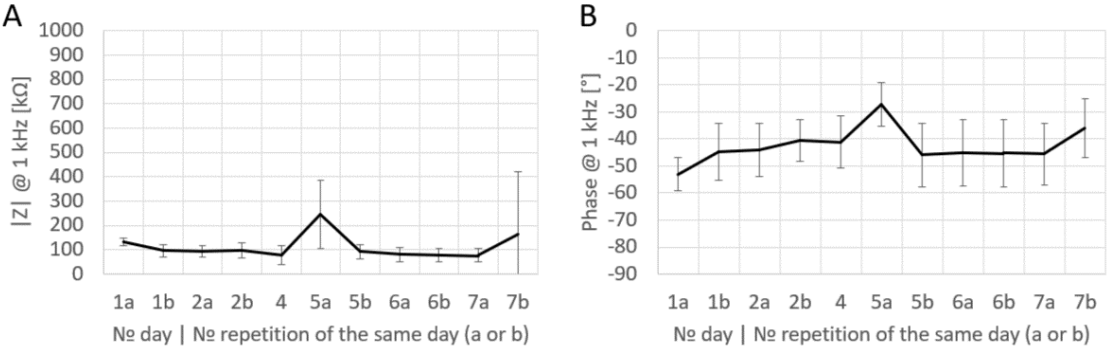
Supplementary Figure S5. Long-term soaking test of the stability of impedance at 1 kHz. The magnitude (A) and phase (B) were measured twice a day for 7 days. Black curves show the average of the 16 sites' impedance, error bars show standard deviation.